https://dx.doi.org/10.1016/j.jcsr.2017.07.012

FE modelling of replaceable I-beam-to-CHS column joints under cyclic loads

Chunyan Quan[1,2], Wei Wang[1,2], Tak-Ming Chan*[,3] and Majd Khador[4]

[1]*State Key Laboratory of Disaster Reduction in Civil Engineering, Tongji University, Shanghai 200092, China*

[2]*Department of Structural Engineering, Tongji University, Shanghai 200092, China*

[3]*Department of Civil and Environmental Engineering, The Hong Kong Polytechnic University, Hung Hom, Kowloon, Hong Kong*

[4]*School of Engineering, The University of Warwick, Coventry, CV4 7AL, United Kingdom*

ABSTRACT

This paper presents a finite element investigation on the structural behavior of replaceable I-beam-to-CHS column joints with external diaphragm plates under cyclic loads. The finite element methodology was validated against complementary experimental results and satisfactory comparisons were observed between numerical and experimental results on the hysteretic curves, initial stiffness, bearing capacity, and energy dissipation. While validating the numerical models, two key parameters – preloading force and bolt hole sizes were identified which have significant effects on the structural performance. Based on the numerical and experimental results, recommendations on the design procedures were proposed.

KEYWORDS Replaceable joint, Hysteretic behavior, Preloading force, Size of bolt holes

1 Introduction

Structures with tubular sections possess many structural and architectural advantages due to their closed geometry. They require less protection against corrosion than comparable structures made with open sections. Another advantage is that the internal void can be used to incorporate ventilation systems or to be filled with concrete. Tubes filled with concrete have higher compression resistance and exhibit excellent seismic performance than hollow counterparts [1]. In terms of design resistances, hollow sections, especially circular hollow sections (CHSs), are very efficient with respect to the torsional stiffness and bending strength in both directions [2] [3]. Overall, although the unit material of tubular columns is more expensive than that of open sections, the former offers a better strength-to-weight ratio that results in more cost-effective moment frames with proper design [2] [4].

As for those connections between circular tubular column and I-Section beam, the connection with outer diaphragm or interior diaphragm is often applied. Experimental results [5] show that the connection with outer diaphragm is more feasible, because the transmission of force is clear, stress distribution of joint region is homogeneous and it is easy to be constructed. It has relatively large stiffness, good plasticity, and high bearing capacity. Several research studies were conducted in the past two decades on external diaphragm connections to tubular columns. Shim et al. [6], Fujimoto et al. [7], Li, et al. [8], and Shin, et al. [9] investigated seismic performance of regular sized outer diaphragm. A non-linear 3D finite element study was conducted by Alostaz et al. [10] on various single-sided connection details between a wide-flange beam and a concrete filled tube column under monotonic loading. AIJ standard for structural calculation of steel reinforced concrete structures [11] and Technical code for concrete filled steel tubular structures (GB50936-2014) [12] have specified design formulas and structural requirements for external

diaphragm connections to tubular columns. According to those relevant formulas, the bearing capacity of connections could be calculated. Two main structural deficiencies of the connections between circular tubular column and I-beam with outer diaphragm are: (i) distortion in the web panel, (ii) strain concentration and out-of-plane failure deformation in the diaphragm plates led to fracture of these plates, welds, and columns [13]. Shifting the beam end away from the CHS face [14, 15] and designing the width and thickness of outer diaphragm for the full strength of beam flanges [16] are recommended for designing joints that will give desired uniform stress flow around and into the CHS column, which will alleviate the two deficiencies aforementioned.

Besides, in steel moment resisting frames (MRFs), a number of welded connections are typically designed to form a plastic hinge at the beam section near the column face. The energy during earthquake can be dissipated by this method, while preventing collapse and ensuring safety [17]. However, the hinges are associated with irrecoverable plastic deformation in the beams, resulting in residual drift angle and heavy economic losses in the repair work after earthquake. Therefore, low damage alternatives have since been developed for use in steel MRFs. For example, a number of researchers have proposed using the unique ability of shape memory alloys (SMA) to undergo large recoverable inelastic strains while dissipating energy in low damage self-centering MRFs whereas the cost of SMA is somewhat higher [18, 19].

As per discussed above, some researchers attempted to obtain a beam-to-CHS column joint with external diaphragm plates, which is practical for construction and most importantly achieves the required structural performance under earthquake for dissipative structures and to avoid permanent deformations in the primary members. One feasible method is to design a joint with built-in replaceable links, which

dissipate most of the seismic energy and act as sacrificial components that can be easily replaced after the earthquake whilst the rest of the joint components remain intact or slightly damaged, to enable a rapid and cost-effective retrofit.

2 Joint construction

2.1 *Design considerations*

To satisfy the requirements mentioned above, Sabbagh et al. [13] proposed a special joint, as shown in Fig. 1. It was designed to avoid fracture in the beam flanges due to local buckling failure and to protect the primary members of the joint under severe seismic actions. The proposed joint is single-sided and includes two collar DPs, which have a 90mm-wide ring, shop-welded to the outer circumference of a 2m CHS 244.5×10 column under sufficient quality control, and bolted to the flanges of a 2m UKB 203×133×30 beam with two tapered cover plates (TCPs) using 24×M22 bolts of Class 10.9. A web stub plate (WS) is welded to the face of the CHS column and connected to the I-beam web using 3×M16 bolts of Class 10.9 to transfer the shear forces. The steel grade of the joint components was S355 in all tests. The only exception was TCPs, which had a steel grade of either S235 or S355

This joint arrangement involved shifting the beam end away from the column face following the recommendations in previous study [10], using cover plates to connect the I-beam flanges to the outer diaphragm plates and bolting the I-beam web to a single-sided web stub plate welded to the CHS column. The middle section of each cover plate was reduced to create a weak section for plastic hinge. The tapered cover plates (TCPs) were designed to reach full plasticity before the I-beam reaches its designing elastic bending resistance to create a multi-fuse energy dissipative mechanism in the joint under seismic loading. Bolt holes in the web stub plate were oversized with the maximum practical clearance and the bolts were

appropriately preloaded to allow slippage in the web connection after the onset of the joint inelastic response. This was to avoid web distortion and localise the failure in the TCPs. The rectangular stiffeners welded longitudinally to the full length of the TCPs was to avoid premature local buckling failure of TCPs. A joint, in which the failure mode was gross plasticity and local buckling of the TCPs and their stiffeners, could be produced through some refined details. Yielding in the TCPs was the main energy dissipation fuse accompanied by bolts slippage in their oversized holes as an extra energy dissipation fuse.

2.2 *Limitations of previous research*

The work of Sabbagh et al. [13] was extended to investigate experimentally the structural performance of this joint under cyclic loading, by Khador [20] and Khador and Chan [21]. Test rig was shown in Fig. 2. The seismic performance of the same joint arrangement through nine full-scale laboratory experiments was investigated, and the influence of certain parameters on the overall hysteretic response and energy dissipation of the joint was examined, as shown in Table 1. The pairs of tapered covered plates (TCPs) used in the nine tests had the same geometry but differed from each other in one or more of the following four parameters. (i) The grade of the TCPs' steel was either S235 or S355, whereas the material of other components was S355. (ii) The size of the bolt holes in the TCPs was either normal/standard round hole (NSH) or oversized round hole (OSH), with clearance of 2 mm or 6 mm respectively. (iii) The TCPs were either stiffened along their longitudinal axis (WS) or not (NS). (iv) The value of the preloading force ($F_{p,Cd}$) acting on the M22 Bolts was either full preloading (FP) or half preloading (HP).

The tests results showed that the joint was a partial-strength semi-rigid joint in all nine tests, according to the joint classification boundaries specified in Eurocode 3: BS EN 1993-1-8 (2005) [22]. The strain and local deformation measurements of different joint components showed that most of them deformed within

the elastic range, except the TCPs, where plastic deformations developed in tapered sections as intended. The experimental results showed that this joint possessed stable hysteretic response, and good ductility if the bolts were properly preloaded.

However, there were a few limitations about the results in this research, due to the available laboratory facilities. The practical displacement-controlled loading cycles in experiments was restricted by the limited loading and displacement capacities of the available actuator in the Structural Laboratory. As a consequence, none of the joints reached its maximum moment resistance or rotational capacity, and the full performances of these joints were not obtained. Besides, obvious bolts' slippage, which is very important for the joint, was not observed and measured in experiments.

Therefore, this research aims to investigate the full performances of these joints through finite element analysis (FEA) using ABAQUS. The measured geometry and the actual material properties of the joints' components in experiments were applied in the finite element models (FEMs). Firstly, the results of the FEMs were validated against the experimental results. Then, FEMs were utilised to further investigate the joint's performance and extend its applicability, especially in terms of how bolts preloading or size of bolt-holes will affect bolts' slippage, and further affect joints' performance. Besides, according to the results from analytical work, relevant design recommendations were proposed.

3 **Finite element modeling methodology**

The software ABAQUS was used in this research. Due to symmetry, only half of the joint was modelled to reduce computational effort, but the dimensions of all components were the same as those in the tests. The proposed joint included two diaphragm plates (DPs), which have a 90 mm-wide ring, welded to the outer circumference of a 244.5×10 circular hollow section (CHS) column and connected to the flanges of

the UKB: 203×133×30 I-beam with two tapered (dog-bone shaped) cover plates (TCPs) using 24×M22 bolts of Class 10.9. A web stub (WS) plate was welded to the face of the CHS column and bolted to the I-beam web with three M16 bolts of Class 10.9 [21].

All components were built using solid elements in finite element models (FEMs). Each model was divided into hexahedron element C3D8R. As for the material constitutive relationships, the yield strain ε_y, the ultimate strength ε_u, the yield strength f_y, and the ultimate strength f_u were shown in Table 2. In FEM, the elastic modulus of most components was chosen from tensile coupon tests, and the elastic modulus of all bolts was assumed as 206 GPa. The Poisson's ratios of all components were 0.3. Mises yield criteria was adopted, and kinematic hardening model was used. The crack was not simulated in FEM. Geometric and material nonlinearities were considered. Increment analysis was adopted to solve geometric nonlinearity. The contact between steel to steel or steel to bolts were defined as follows. Tangential behavior was "penalty function", and normal behavior was "hard contact". The friction coefficient was dependent on the specified class of surface treatment. For class C surfaces used in experiments, which are cleaned by wire brushing or flame cleaning, with any loose rust removed, this friction coefficient equals to 0.3, as given in Eurocode 3: BS EN 1993-1-1 (2005) [23]. And "tie" was used to simulate the weld. The schematic arrangement of the FE model was shown in Fig. 3. The boundary conditions of the FE models were the same as the experimental specimens. For example, the boundary conditions of the CHS column were assumed to be hinges in the design of the specimen to allow rotation at the column ends during experiments. Two hinges were designed and connected to the ends of the specimen's beam. Vertical displacement-controlled loading was imposed at the end of specimen's I-beam. In order to avoid over-constrained condition, a rigid plate (thickness of 5 mm) was set at column end and beam end respectively,

and they were “tie” with column or beam. As shown as circles in Fig. 3, the out-of-plane deflection (Z-direction) of beam flanges was constrained to simulate the lateral support. The whole procedure of loading was divided into 7 general steps. At the beginning, if there were no constraints on the TCPs, the analysis could not be submitted. Therefore, the temporary constraint near the connection was applied in the first step, meanwhile all bolts were fastened with 10 N so as to build contact among every part. Then, the temporary constraints were released in the second step. The gravity of all components was applied from the third step. Pre-tensioning forces of the bolts were imposed in step three to six, quarter in each step, in order to avoid numerical abortion due to sudden change in forces. In the seventh step, fixing bolts at current length should be used, which means at the beginning of this step, the current lengths of bolts were preserved, afterwards the length and force of bolts would change along with applied loading correspondingly. Meanwhile, the vertical displacement of beam end was imposed in the seventh step, adhering to same loading protocol as experiment, which was based on the ANSI/AISC 341-10 (2010) provisions [24] for qualifying cyclic tests of beam-to-column moment connections. In order to investigate the behavior of joint further, in FEM, the maximum interstorey drift angle θ_{dr} was designed to be up to 0.04 rad, as shown in Fig. 4 and Table 3.

4 **Validation of FEM**

4.1 *Hysteretic response*

As shown in Fig. 5, L_{eff} is beam’s effective length, which represents the distance between beam end and the section where the connection moment is calculated. L_{cr} is beam’s critical length. M_{con} is the connection moment, which refers to weakest section of the joint. The design elastic bending resistance of the I-beam’s cross section about its major axis y-y $M_{b,el,y,Rd}$ is 117.6 kN·m in this research. In following hysteretic curves,

y-axis is the ratio of M_{con} to $M_{b,el,y,Rd}$, and x-axis was the rotation of the plastic hinge region θ_{con}. For joints in dissipative moment resisting frames, BS EN 1998-1: 2004 [25] specifies in Clause 6.6.4 (5) that the column web panel elastic deformation should not be included in the evaluation of the rotation capacity of the plastic hinge region. Since the web panel and web stub deformed elastically in all tests, the rotations of the plastic hinge region θ_{con} were obtained by subtracting the inclination measurements of INC-2 from those of INC-3 to exclude the elastic deformations of the column web panel and the web stub [20], as shown in Fig. 5. Mises stress contours of FEMs are also presented.

In order to compare clearly, all FEMs were loaded up to same drift angle with the experiments. As shown in Fig. 6, the trend of hysteretic curves of most FEMs basically agreed well with experiments, except Test-8 and Test-9, which will be discussed further in the following sub-section. In addition, The asymmetry shown in Test-4 may be attributed to the geometric imperfection.

In FEM-5 and FEM-7, up to θ_{dr} +0.02 rad, most components still stayed elastic, as shown in Fig. 7b. In other FEMs, TCPs yielded and buckled, and the stress of beam flange in critical section was higher, and other components still kept elastic or slight damage, such as FEM-6 in Fig. 7a, in which the failure mode was consistent with experiment, as shown in Fig. 8. To get a better view, corresponding sub-contours are also highlighted for FEM-1. In the sub-figure Fig. 9, black shade means yielding, and white shade means elastic. Up to θ_{dr} : +0.04 rad, TCPs yielded; column still remained elastic; beam presented minor yielding near the bolt hole and contact surface with DP; web stub showed minor yielding at the corner; DPs displayed minor yielding near the bole hole.

4.2 *Initial stiffness*

Eurocode 3: BS EN 1993-1-8 (2005) [22] defines the rotational stiffness of a joint as the moment

required to produce unit rotation in that joint. The initial rotational stiffness, $S_{j,ini}$, of each joint in this project was obtained by calculating the slope of the linear part of the moment-rotation curve of the joint. In the joint moment-rotation curves, joint moments were calculated at the connected end of the I-beam, and joint rotations were obtained from the measurements of INC–3, which included the elastic rotation of the column web panel and the web stub, as shown in Fig. 5. Table 4 presents the calculated initial rotational stiffness of nine joints. Eurocode 3: BS EN 1993-1-8 (2005) [22] classifies joints according to their initial rotational stiffness as rigid, semi-rigid or pinned. The classification boundaries specified for rigid and pinned joints are 36.7 kN·m/mrad and 0.7 kN·m/mrad respectively. Therefore, all these nine joints were classified as semi-rigid joints.

4.3 *Strength classification*

It is illustrated in Eurocode 3: BS EN 1993-1-8 (2005) [22] that a joint may be classified as full-strength, nominally pinned or partial strength by comparing its design moment resistance with the design moment resistances of the members that it connects. According to the design theory of this joint, the plastic moment resistance of column must be higher than beam, thus the maximum joint moment $M_{con,max}$ was normalised by the design plastic bending resistance of beam ($M_{b,pl,y,Rd}$ = 145 kN·m) in Table 5. The FEM results show that the joint was a partial-strength joint in all nine FEMs as same as experimental results. In fact, this result is inevitable, because in the design methodology of this joint, a very important step is to ensure the beam owning sufficient overstrength to remain elastic before TCPs reach full plasticity.

4.4 *Energy dissipation*

Accumulated energy dissipation values at the end of each loading cycle were obtained for all tests by calculating the areas enclosed by the moment-rotation hysteresis loops. The energy dissipation mainly

came from the onset of yield in the TCPs, slip in the connection or both. Table 6 shows the comparison between test and FEM about accumulated energy dissipation of joint at the end of last cycle in experiments.

5 **Parametric Investigation**

Last section presented the comparison between experimental and numerical results on hysteretic response, initial stiffness, strength classification, and energy dissipation. The replaceability of these joints has been proved to be achievable by keeping most joint components in the elastic range or slightly damaged, except TCPs. All joints were classified as semi-rigid and partial-strength joints. After the validation of FEMs, this session will indicate some further investigations.

5.1 *Bolts preloading force*

5.1.1 S355-OSH-WS-FP/ HP/ 35%P

As shown in Fig. 6, it can be observed that the hysteretic curves of most tests were in good agreement at both the peak and the postpeak stage, except Test-8 and Test-9. The moment values of FEM-9 were higher than Test-9. Fig. 10 shows that the comparison between FEM-5 and FEM-9, ended with θ_{dr} 0.04 rad. In Test-5 and Test-9, the TCPs were identical in all parameters except the preloading force acting on their bolts. The TCPs' bolts in Test-5 were fully preloaded (FP), whereas the TCPs' bolts in Test-9 were preloaded to half of that value (HP). The value of the full preloading force ($F_{p,Cd}$) acting on them was designed in line with Eurocode 3: BS EN 1993-1-8 (2005) [22] for slip-resistant connections:

$$F_{p,Cd} = 0.7 \times f_{ub} \times A_s \quad (1)$$

where f_{ub} is ultimate strength of the M22 bolts; A_s is the tensile stress area of a bolt. Fig. 10 shows that the values of connection moments in FEM-5 were higher than FEM-9, as a direct consequence of higher preloading forces in FEM-5. This indicates that the preloading force acting on bolts in Test-9 may not

reach anticipated half of the full preloading force.

Fig. 11 shows the normalized moment-rotation curves of the connection in Test-9 and FEM-9. Besides, there is another hysteretic curve of a new FEM, named FEM-9.1 S355-OSH-WS-35%P, which was identical with Test-9 in all parameters, except that the preloading force on bolts were only 35% of full preloading. It can be seen that, when the preloading force acting on TCPs' bolts decreased to 35%, the hysteretic curve would coincide with the results from Test-9.

The hysteretic curves of three models FEM-5, FEM-9, and FEM-9.1 indicate that, the connection with lower preloading force of TCPs' bolts led to higher rotation capacity. In Fig. 12, black shade means yielding, and white shade means elastic. It shows that lower preloading force of TCPs' bolts reduced stress demands on DPs and beam flange. However, due to the increase of rotation, the stress near the lowest bolt hole on beam web was higher on account of bearing stress on hole wall.

In FEM-5, FEM-9, and FEM-9.1, up to θ_{dr} 0.04 rad, the maximum joint moment $M_{con,max}$ was 124.0, 87.8, 74.3 kN·m respectively. The connection with lower preloading force of TCPs' bolts resulted in the bearing capacity decreased. Accumulated energy dissipation of three models were 11.20, 18.96, 19.07 kN·m·rad respectively, which indicates that reducing the bolts' preloading force resulted in the connection dissipating more energy, due to the activation of connection slip. In order to present the connection slip more clearly, a reference point (RP) was chosen on the contact surface between one bolt head and TCP to describe slippage, as shown in Fig. 13. The relative displacement between the bolt and TCP in the direction of X-axis (parallel to beam) was calculated by subtracting the displacement of RP on the TCP from the displacement of the bolt head at the same location. Fig. 14 shows this relative displacement versus drift angle θ_{dr} of three FEMs. At the same drift angle, higher relative displacement means more slippage. It can

be seen that reducing preloading force of TCPs' bolts facilitated slippage between bolts and TCP. This was consistent with the formula in the Eurocode 3: BS EN 1993-1-8 (2005) [22], in which the design slip resistance of the bolt group $F_{s,Rd}$ is directly proportional to bolts' preloading force.

5.1.2 S235-OSH-NS-FP/ HP/ 40%P

In Fig. 6, it can be seen that the moment values obtained from FEM-8 were higher than Test-8. The comparison of FEM-5, FEM-9 and FEM-9.1 indicates that this may be attributed to the level of preloading forces on TCPs' bolts. Therefore, this section shows the comparison between FEM-1 S235-OSH-NS-FP, FEM-8 S235-OSH-NS-HP, and a new FE model FEM-8.1 S235-OSH-NS-40%P, which was identical with Test-8 in all parameters, except that the preloading force on bolts were only 40% of full preloading. Fig. 15 reveals if the preloading force acting on TCPs' bolts in FEM-8.1 decreased to 40%, the hysteretic curve shows better agreement with the results from Test-8.

As same as the conclusion of last pair of comparison, the connection with lower preloading force of TCPs' bolts led to higher rotation capacity, as shown in Fig. 16. And Fig. 17 presents that lower preloading force of TCPs' bolts reduced stress demands on DPs and beam flange, but the stress near the lowest bolt hole on beam web was higher on account of bearing stress on hole wall.

In FEM-1, FEM-8, and FEM-8.1, up to θ_{dr} 0.04 rad, the maximum joint moment $M_{con,max}$ was 95.7, 74.6, 67.4 kN·m respectively, and accumulated energy dissipation of three models were 14.17, 19.36, 19.70 kN·m·rad respectively. This indicates that reducing the bolts' preloading force resulted in lower bearing capacity, but higher energy dissipation due to the activation of connection slip, as shown in Fig. 18.

However, the most important is how to control exact preloading force on TCPs' bolts. As shown in

subsection 5.1.1, an essential problem is the preloading force in practical use may be not applied as planned, which has significant influence on the behavior of connection. Therefore, the measurement about controlling the exact value of preloading force in practice is a precondition to utilize this change.

5.2 *Size of bolt-holes*

From section 4, it can be found the accumulated energy dissipation and bearing capacity of joint with either standard sized bolt holes or oversized bolt holes were different prominently, such as the comparison between Test-1 and Test-6. According to Eurocode 3: BS EN 1993-1-8 (2005) [22], the design slip resistance of the bolt group $F_{s,Rd}$ is directly proportional to a coefficient k_s that depends on the hole size. Therefore, the size of bolt holes would affect the behavior of connections. Here below shows two pairs of models in which the TCPs were identical in all parameters but the size of their bolt's holes for comparison.

5.2.1 S235-OSH/NSH/SSH-WS-FP

The first comparison was between FEM-2 S235-OSH-WS-FP, FEM-3 S235-NSH-WS-FP, and a new FE model FEM-3.1 S235-SSH-WS-FP, which was identical with Test-3 in all parameters, except the size of bolt holes. Fig 19 shows the shapes of TCPs in three models. The bolts' holes of the TCPs in FEM-3 were normal/standard round holes (NSH) of size ($d_0 = d$ +2 mm = 24 mm, where d is the diameter of bolt), whereas the holes of the TCPs in FEM-2 were oversized round holes (OSH) with 6 mm clearance ($d_0 = d$ +6 mm = 28 mm), and the size of TCPs' bolt holes in FEM-3.1 was slotted (SSH) with 24 mm-width and 40 mm-length, according to ANSI/AISC 360-10 (2010) [26].

Fig. 20 shows the Mises stress of these three models, which reveals that OSH-TCPs and SSH-TCPs resulted in lower stress demands on the I-beam and DPs, especially SSH-TCPs. Fig. 21 reveals that NSH-TCPs resulted in a stronger connection and lower rotation capacity. In FEM-2, FEM-3, and FEM-3.1, up

to θ_{dr} 0.04 rad, the maximum joint moment $M_{con,max}$ was 116.3, 121.0, 106.9 kN·m, respectively and accumulated energy dissipation of three models were 12.59, 7.58, 14.67 kN·m·rad respectively. This indicates that TCPs with slotted holes resulted in lower bearing capacity, but higher energy dissipation due to the activation of connection slip, as shown in Fig. 22.

5.2.2 S355-OSH/NSH/SSH-NS-FP

This section compares results between FEM-4 S355-OSH-NS-FP, FEM-7 S355-NSH-NS-FP, and a new FE model FEM-7.1 S355-SSH-NS-FP, which was identical with Test-7 in all parameters, except for the size of bolt holes.

Fig. 23 shows the Mises stress of these three models, which reveals that OSH-TCPs and SSH-TCPs resulted in lower stress demands on the I-beam and DPs, especially SSH-TCPs. Fig. 24 reveals that NSH-TCPs resulted in a stronger connection and lower rotation capacity. In FEM-4, FEM-7, and FEM-7.1, up to θ_{dr} 0.04 rad respectively, the maximum joint moment $M_{con,max}$ was 105.6, 111.5, 98.4 kN·m respectively, and accumulated energy dissipation of three models were 12.86, 8.37, 13.30 kN·m·rad respectively. This indicates that TCPs with slotted holes resulted in lower bearing capacity, but higher energy dissipation due to the activation of connection slip, as shown in Fig. 25.

6 **Design methodology**

The hysteretic behavior mainly aims at working mechanism of a joint, and design methodology points at practical application. Reasonable design philosophy is the basis of attaining a joint that is practical for construction and achieves required structural performance under seismic loading for dissipative structures. Above sections indicate that the most important characteristics of this joint are reliable hysteretic behavior and replaceability. To realize these two parts, following design procedures are recommended.

As shown in Fig. 26, firstly, the internal force of this joint, which could not surpass the resistance, could be calculated with exterior loading applied on frame. Next, calculate the design plastic resistance of the cross section of the tapered region as the resistance force of this joint, which agrees with the design concept of developing a plastic region in the TCP's reduced section area before any failure in the other sections of the TCP. Then, the I-beam in this joint is assumed to be a non-dissipative member, thus its maximum strength is limited to the design elastic bending resistance $M_{b,el,y,Rd}$. Afterwards, design the connection between TCP and beam flange to allow slip to be activated beyond the serviceability limit to act as an extra seismic energy dissipation fuse and delay the yield onset in the beam. Besides, DP, column, web stub and other connections are all designed to have sufficient overstrength for the full elastic strength of the beam so that they can remain elastic.

6.1 *TCP*

The reduced section area of the tapered cover plates (TCPs) is designed to be the main dissipative zone in the joint. Therefore, this area should yield before other zones in the joint leave their elastic range. Furthermore, for the TCP to act as the sacrificial replaceable component of the joint, plastic region should develop in its tapered section under cyclic loading before yield onset in any other joint component.

Through the comparison between FEM-1 S235-OSH-NS-FP and FEM-4 S355-OSH-NS-FP, as shown in Fig. 27, it can be found that S235-TCPs resulted in lower bearing capacity, but higher rotation capacity. Meanwhile, FEM-1 with S235-TCPs had lower stress demands on the I-beam and DPs, as shown in Mises stress contours aforementioned. Besides, up to drift angle θ_{dr} 0.04 rad, the accumulated energy dissipation of FEM-1 and FEM-4 was 14.17 and 12.86 kN·m·rad respectively. This means the connection with S235-TCPs had higher energy dissipation. Therefore, S235 is recommended for the steel grade of TCP. When

the design plastic resistance of the cross section of the tapered region is calculated, the yield strength of the TCP is multiplied by 1.1, because this is the intended plastic zone under seismic loads. From this perspective, it pose potentially challenge if one chooses S355 as TCPs' material, as same as other components' material. Especially if the true yield strength of TCP may be higher than its nominal yield strength, it would be difficult to guarantee TCP yields ahead of beam. If the resistance of connection with S235 TCPs is lower than exterior loading, another option is to use S275 steel.

As shown in Fig. 28, the comparison between the pair of connection FEM-2 with stiffeners and FEM-1 without stiffeners illustrates that vertical stiffeners resulted in a stronger connection with higher bearing capacity, but weaken rotation capacity. Besides, up to drift angle θ_{dr} 0.04 rad, the accumulated energy dissipation of FEM-1 and FEM-2 was 14.17 and 12.59 kN·m·rad respectively. This means the connection without vertical stiffeners resulted in higher energy dissipation. Furthermore, the most important problem is the difficulty for the construction of concrete floor and steel reinforcement, if there are stiffeners.

The design tension resistance of TCP $N_{TCP,t,Rd}$ equals to the minimum of the design plastic resistance of the gross section $N_{pl,Rd}$, the design plastic resistance of the reduced section $N_{red,pl,Rd}$, and the design ultimate resistance of the net cross-section at holes for bolts $N_{u,Rd}$. If the design tension resistance of TCP $N_{TCP,t,Rd}$ equals to $N_{red,pl,Rd}$, it will agree with the design concept of developing a plastic region in the TCP's reduced section area before any failure in the other sections of the TCP. The size of bolt holes in the TCP does not affect its design tension resistance because the latter is governed by the resistance of the reduced section area.

6.2 *Beam*

The recommended grade of the beam's steel is S355. The I-beam in this joint is assumed to be a non-

dissipative member in seismic events, thus its maximum strength is limited to the design elastic bending resistance $M_{b,el,y,Rd}$. To allow the reduced section of TCP to reach full plasticity before the yield onset at the critical section of the I-beam, the inequality $M_{con,pl} < M_{con,b,el}$ should be satisfied, where $M_{con,pl}$ is the connection moment when the reduced section area of TCP reaches full plasticity, and $M_{con,b,el}$ is the connection moment when the beam's critical section reaches its design elastic bending resistance, as shown in Fig. 5.

6.3 *The connection between TCP and beam flange*

In the proposed joint arrangement, the tapered cover plate is connected to I-beam flange using a group of six M22 bolts of grade 10.9. The connection is loaded in shear during the cyclic bending of the beam and the bolts are pre-tensioned to have a Category–B connection that is slip resistant at the serviceability limit state, according to Eurocode 3: BS EN 1993-1-8 (2005) [22]. This is to allow slip to be activated beyond the serviceability limit to act as an extra seismic energy dissipation fuse and delay the yield onset in the beam. $F_{s,Rd}$ is the corresponding design slip resistance of the bolt group. Connection slip should occur before the full plasticity of the reduced section area of the TCP, that means $F_{s,Rd} < N_{TCP,t,Rd}$. This is to ensure that slip is activated to create a second seismic energy dissipation fuse. The connection slip resistance is also checked against the serviceability limit shear load so that slip is activated beyond it.

The design slip resistance of the bolt group $F_{s,Rd}$ is directly proportional to bolts' preloading force. In section 5.1, it can be seen that, the preloading force of TCPs' bolts has a great effect on joints' behavior. Generally, reducing preloading force results in lower bearing capacity of connection, but this could promote rotation capacity and energy dissipation, due to the activation of bolts' slippage. As a result, in order to design a joint with higher bearing capacity, full preloading force could be applied on bolts. In

contrast, if a joint is designed to dissipate more energy, reduce stress demands on other components, better rotation capacity, reducing the preloading force on TCPs' bolts is an ideal method. However, if the preloading force of bolts is decreased, the connection may slip earlier, which could not meet the criteria that slip resistant at serviceability limit state. But this does not change the result that TCPs reach full plasticity before the yield onset at the critical section of the I-beam. As for this method, a very important issue is how to control the exact value of bolts' preloading force in practice. This can be solved by a special torque wrench available in mechanical manufacturing, which links the preloading force and torque. In future experiments, in order to improve monitoring of the bolts' preloading force, some strain gauges can be fixed up on bolts to control preloading force more precisely.

The design slip resistance of the bolt group $F_{s,Rd}$ is also directly proportional to a coefficient k_s that depends on the hole size. In section 5.2, it can be found that the connection with SSH-TCPs (slotted bolt holes) results in lower bearing capacity, but its ability to dissipate energy and rotation capacity is higher than the one with OSH-TCPs (oversized bolt holes) or NSH-TCPs (normal sized bolt holes), especially NSH-TCPs, because of the connection slip. Therefore, if the bearing capacity of joint can resist exterior loading, slotted bolt holes should be selected in preference.

From Fig. 6, which shows the hysteretic response of Test-8, it can be seen that the connection rotation of this joint both in experiment and FEM exceeded the minimum rotation capacity required for plastic hinge regions in medium ductility class (DCM) structures, which is 25 mrad, specified by Eurocode 8: BS EN 1998-1 (2004) [25]. Therefore, if appropriate bolts preloading force, suitable size of bolt holes and material grade are applied for TCP, the rotation capacity of joint will be improved to reach DCM structures, such as FEM-8 and FEM-8.1. Or even it will reach high ductility class (DCH) structures, which is 35 mrad,

if further loading, because there was no strength or stiffness degradation of these joints greater than 20% in any of their moment-rotation curves.

As shown in Fig. 9, the stress on the contact surface between beam flange and DP was higher. Because when the drift angle increased to a certain degree, beam flange and DP touched with each other. Considered from this angle, leaving a gap between beam flange and DP is suggested to avoid the contact.

6.4 *Other components and connections*

The column is designed to remain elastic for the full elastic strength of the beam. Both of the design bending resistance of the column and the design plastic shear resistance of the column web panel should be checked.

The geometry of the diaphragm plates (DPs) is chosen in line with the findings of Sabbagh et al. [13] to provide uniform stress flow around the CHS column and avoid stress concentration in them that could lead to their failure or weld fracture. In this research, the DPs should be designed to have sufficient over-strength for the full elastic strength of the beam so that they could remain elastic. The bending moment of the I-beam was assumed to be fully transmitted through tapered cover plates into the diaphragm plates. The design tension resistance of the diaphragm plate should be checked at three cross sections: the rectangular section, the cross section at the column face and the ring cross section.

The web stub is subject to the shear force transferred from the I-beam web through the web connection, and it should be designed for the full elastic strength of the beam. The main checks carried out for the web stub are the design shear resistance, the design block tearing resistance.

The web connection is loaded in shear during the bending of the beam. The bolts are placed in oversized holes in the web stub plate with the maximum practical clearance and they are appropriately preloaded to

have a slip resistant connection in which slippage in the web connection would occur after the onset of the inelastic joint response. However, as shown in Fig. 12, due to the increase in rotation, the stress near the lowest bolt hole on beam web was higher on account of bearing stress on hole wall. This can be avoided by designing slotted or oversized shape as the lowest bolt hole on beam web.

7 Conclusions

This paper has presented a finite element modelling of a replaceable join between circular hollow section column and I-section beam under cyclic loads. The following concluding remarks were observed in this research:

(1) The results of the FEMs were validated against the experimental results on hysteretic curves, initial stiffness, bearing capacity, and energy dissipation. Most results from FEMs basically agreed well with the experiments.

(2) The built-in replaceable links in proposed joint can dissipate seismic energy and act as sacrificial components that can be easily replaced after a seismic event whilst the rest of the joint components remain intact or slight damage, thus minimize the operations and time of repair for post-seismic damages of the structure.

(3) Preloading force of TCPs' bolts has a great effect on joints' behavior. Generally, reducing preloading force resulted in lower bearing capacity, but lower stress demands on DPs and beam flange, higher rotation capacity and energy dissipation due to the activation of bolts' slippage. However, the most important issue is how to control the exact preloading force on TCPs' bolts in practice.

(4) The connection with SSH-TCPs (slotted bolt holes) results in lower bearing capacity, but its ability to dissipate energy and rotation capacity is higher than the one with OSH-TCPs (oversized bolt holes) or

NSH-TCPs (normal sized bolt holes), especially NSH-TCPs, because of the connection slip.

(5) To realize reliable hysteretic behavior and replaceability of this joint, some design recommendation were proposed, including the material, preloading force of bolts and shapes of bolt holes, according to the finite element results together with the experimental results.

Acknowledgements

The authors are grateful for the support from the National Science Foundation of China (NSFC/51378380) and the Engineering and Physical Science Research Council (EP/1020489/1). The financial support from the Hong Kong Polytechnic University (PolyU: G-UC75/G-YBHV) is also gratefully acknowledged.

References

[1] Quan C, Wang W, Zhou J, et al. Cyclic behavior of stiffened joints between concrete-filled steel tubular column and steel beam with narrow outer diaphragm and partial joint penetration welds. Frontiers of Structural and Civil Engineering, 2016, 10(3):333-344.

[2] Kurobane Y, Packer J A, Wardenier J, Yeomans. Design guide for structural hollow section column connections. CIDECT 9; 2004.

[3] Chan T M, Gardner L. Bending strength of hot-rolled elliptical hollow sections. Journal of Constructional Steel Research, 2008, 64(9):971-986.

[4] Elghazouli A Y, Málaga-Chuquitaype C, Castro J M, et al. Experimental monotonic and cyclic behaviour of blind-bolted angle connections. Engineering Structures, 2009, 31(11):2540-2553.

[5] Choi S M, Shin I B, Eom C H, Kim D K, Kim D J. Elasto-plastic behavior of the beam to concrete filled circular steel column connections with external stiffener rings, Griffith University Gold Coast Campus. Building for the 21st Century, Australia; 1995.

[6] Shim J S, Han D J, Kim K S. An experimental study on the structural behaviors of H-shaped steel beam-to-concrete filled steel square tubular column connections. Building for the 21st Century, Australia; 1995.

[7] Fujimoto T, Inai E, Kai M, et al. Behavior of beam-to-column connection of CFT column system. Proc, 2000.

[8] Li X, Xiao Y, Wu Y T. Seismic behavior of exterior connections with steel beams bolted to CFT columns. Journal of Constructional Steel Research, 2009, 65(7):1438-1446.

[9] Shin K J, Kim Y J, Oh Y S. Seismic behaviour of composite concrete-filled tube column-to-beam moment connections. Steel Construction, 2008, 64(1):118-127.

[10] Alostaz Y M, Schneider S P. Analytical behavior of connections to concrete-filled steel tubes. Journal of Constructional Steel Research, 1996, 40(2):95-127.

[11] AIJ. AIJ standard for structural calculation of steel reinforced concrete structures. Architectural Institute of Japan; 2001.

[12] GB50936-2014. Technical code for concrete filled steel tubular structures; 2014.

[13] Sabbagh A B, Chan T M, Mottram J T. Detailing of I-beam-to-CHS column joints with external diaphragm plates for seismic actions. Journal of Constructional Steel Research, 2013, 88(9):21-33.

[14] Alostaz Y M, Schneider S P. Connections to concrete-filled steel tubes. Structural Engineering Series No. 613, University of Illinois at Urbana-Champaign; 1996.

[15] Schneider S P, Alostaz Y M. Experimental Behavior of Connections to Concrete-filled Steel Tubes. Journal of Constructional Steel Research, 1998, 45(3):321-352.

[16] Wang W, Chen Y, Li W, et al. Bidirectional seismic performance of steel beam to circular tubular column connections with outer diaphragm. Earthquake Engineering & Structural Dynamics, 2011, 40(10):1063-1081.

[17] Roeder C W. Connection Performance for Seismic Design of Steel Moment Frames. Journal of Structural Engineering, 2002, 128(128):517-525.

[18] Wang W, Chan T M, Shao H. Seismic performance of beam–column joints with SMA tendons strengthened by steel angles. Journal of Constructional Steel Research, 2015, 109:61-71.

[19] Wang W, Chan T M, Shao H, et al. Cyclic behavior of connections equipped with NiTi shape memory alloy and steel tendons between H-shaped beam to CHS column. Engineering Structures, 2015, 88:37-50.

[20] Khador M. Cyclic behavior of external diaphragm joint between steel I-section beam and circular hollow section columns. PhD Thesis: The University of Warwick; 2015.

[21] Khador M, Chan T. Cyclic behaviour of external diaphragm joint to CHS column with built‐in replaceable links. Steel Construction, 2016, 9(4):331-338.

[22] Eurocode 3: Design of steel structures: part 1-8: Design of joints, EN 1993-1-8; 2005.

[23] Eurocode 3: Design of steel structures: part 1-1: General rules and rules for buildings, EN 1993-1-1; 2005.

[24] ANSI/AISC 340-10. Seismic provisions for structural steel buildings: American Institution of Steel Construction; 2010.

[25] Eurocode 8: Design of structures for earthquake resistance: part 1: General rules, seismic actions and rules for buildings, EN 1998-1; 2004.

[26] ANSI/AISC 360-10. Specification for structural steel buildings: American Institution of Steel Construction; 2010.

List of Figure Captions

Fig. 1 The components of the beam to column joint

Fig. 2 Schematic arrangement of the test rig [20]

Fig. 3 FE model

Fig. 4 Calculation of the actuator's displacements for the loading protocol

Fig. 5 Moment of the connection in relation to the beam's moment

Fig. 6 Normalised moment-rotation curves of nine tests

Fig. 7 Mises stress contours of FEM-6 and FEM-7

Fig. 8 Buckling of top TCP in Test-6 [20]

Fig. 9 Mises stress contours of main components in FEM-1 S235-OSH-NS-FP (θ_{dr} : +0.04 rad)

Fig. 10 Normalised moment-rotation curves of FEM-5 and FEM-9, θ_{dr} 0.04 rad

Fig. 11 Normalised moment-rotation curves of Test-9, FEM-9 and FEM-9.1, θ_{dr} 0.04 rad

Fig. 12 Mises stress contours of beam and DPs in FEM-5, FEM-9, FEM-9.1 (θ_{dr} : +0.04 rad)

Fig. 13 RP was defined to describe relative displacement between bolt and TCP

Fig. 14 Relative displacement between bolt and TCP in FEM-5, FEM-9, FEM-9.1

Fig. 15 Normalised moment-rotation curves of Test-8, FEM-8 and FEM-8.1, 29 cycles

Fig. 16 Normalised moment-rotation curves of FEM-1, FEM-8, FEM-8.1, θ_{dr} 0.04 rad

Fig. 17 Mises stress contours of beam and DPs in FEM-1, FEM-8, FEM-8.1 (θ_{dr} : +0.04 rad)

Fig. 18 Relative displacement between TCP's bolt and bolt hole in FEM-1, FEM-8, FEM-8.1

Fig. 19 The sketches of TCP in FEM-2, FEM-3, FEM-3.1

Fig. 20 Mises stress contours of beam and DPs in FEM-2, FEM-3, FEM-3.1 (θ_{dr} : +0.04 rad)

Fig. 21 Normalised moment-rotation curves of FEM-2, FEM-3, FEM-3.1, θ_{dr} 0.04 rad

Fig. 22 Relative displacement between TCP's bolt and bolt hole in FEM-2, FEM-3, FEM-3.1

Fig. 23 Mises stress contours of beam and DPs in FEM-4, FEM-7, FEM-7.1 (θ_{dr} : +0.04 rad)

Fig. 24 Normalised moment-rotation curves of FEM-4, FEM-7, FEM-7.1, θ_{dr} 0.04 rad

Fig. 25 Relative displacement between TCP's bolt and bolt hole in FEM-4, FEM-7, FEM-7.1

Fig. 26 Design flow

Fig. 27 Normalised moment-rotation curves of the connection in FEM-1, FEM-4, θ_{dr} 0.04 rad

Fig. 28 Normalised moment-rotation curves of the connection in FEM-1, FEM-2, θ_{dr} 0.04 rad

List of Table Captions

Table 1 Tests titling according to the type of TCPs used in the test specimens [20]

Table 2 Key results from the tensile coupon tests [21]

Table 3 Loading protocol

Table 4 Initial rotational stiffness of the joints

Table 5 Joint moment of nine tests

Table 6 Accumulated energy dissipation of joints

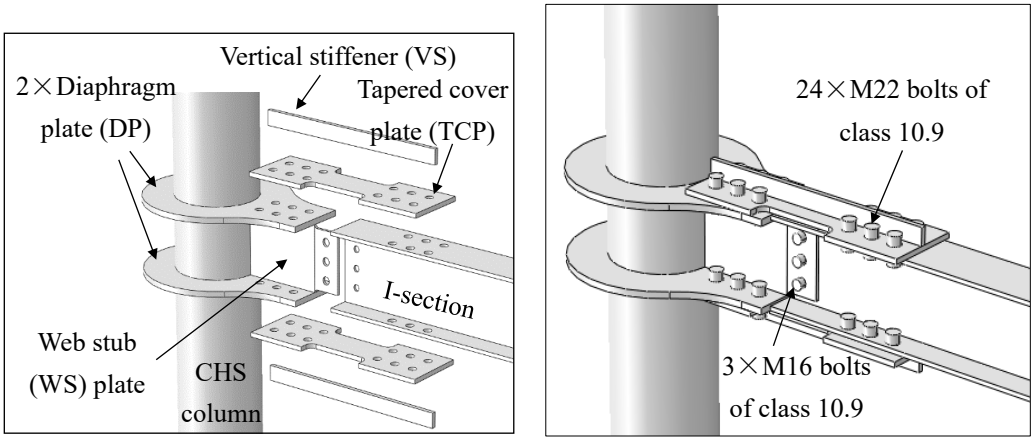

(a) Before assembly (b) After assembly

Fig. 1 The components of the beam to column joint

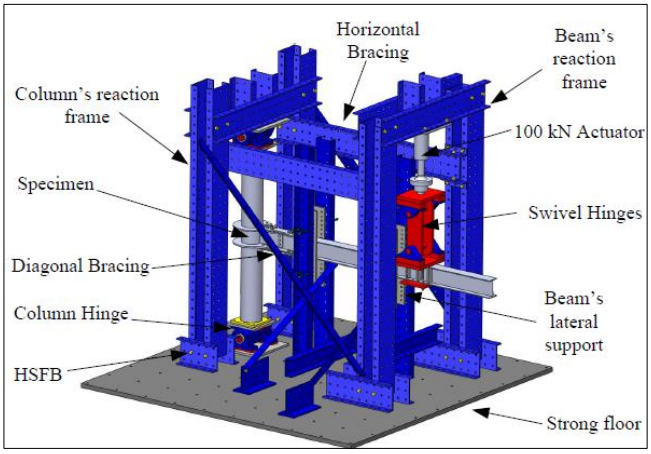

Fig. 2 Schematic arrangement of the test rig [20]

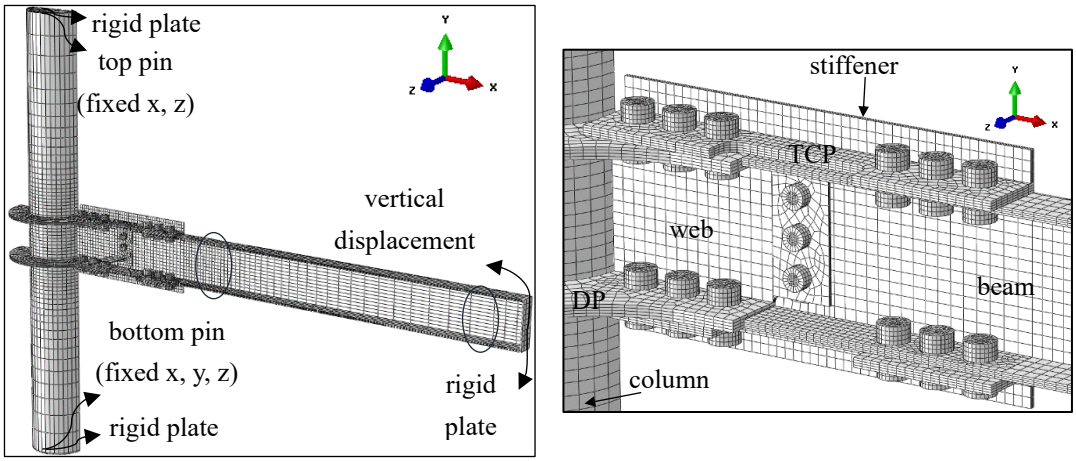

(a) Boundary conditions and loading direction (b) Detailed model

Fig. 3 FE model

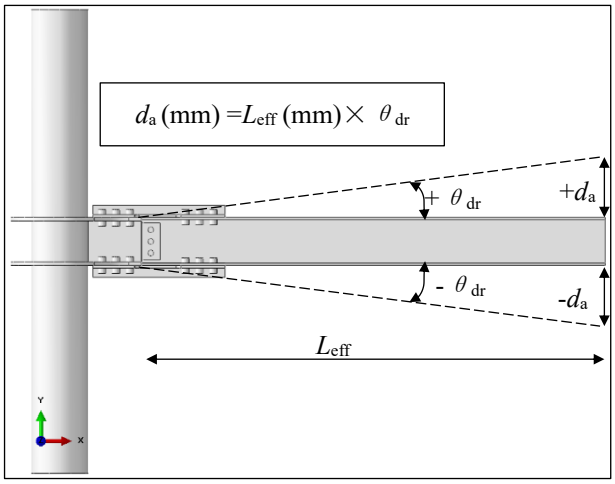

Fig. 4 Calculation of the actuator's displacements for the loading protocol

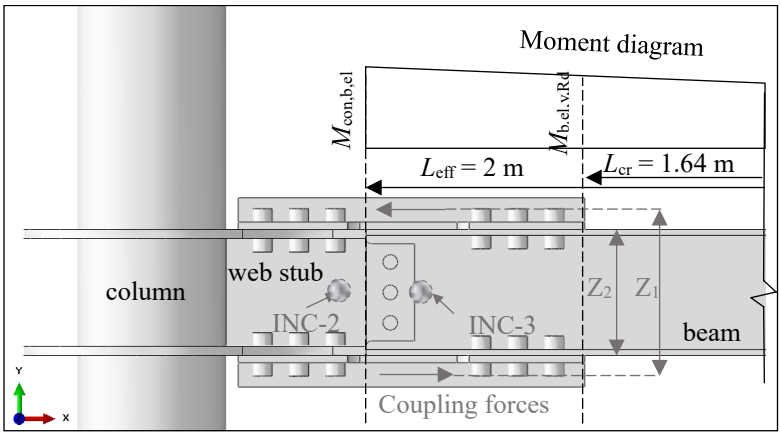

Fig. 5 Moment of the connection in relation to the beam's moment

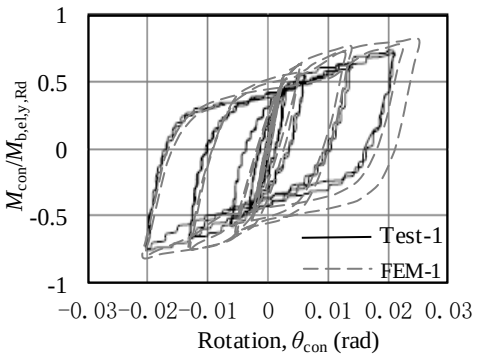

(a) Test-1 S235-OSH-NS-FP, θ_{dr} : 0.04 rad

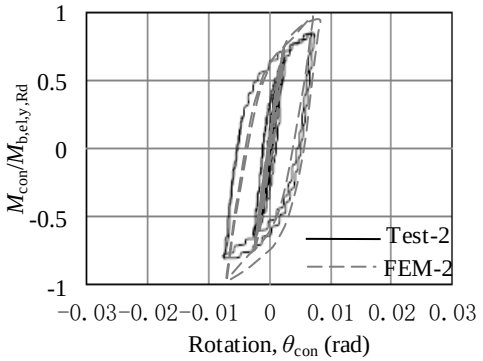

(b) Test-2 S235-OSH-WS-FP, θ_{dr} : 0.03 rad

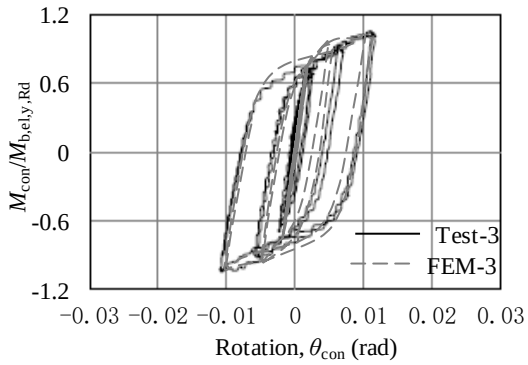

(c) Test-3 S235-NSH-WS-FP, θ_{dr} : 0.04 rad

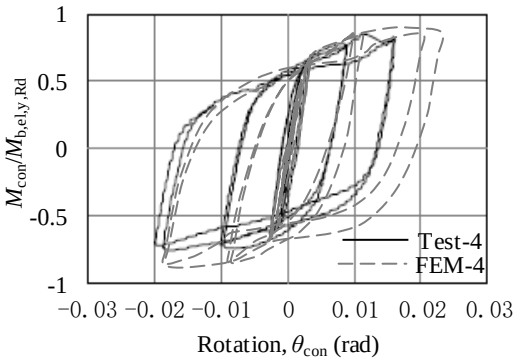

(d) Test-4 S355-OSH-NS-FP, θ_{dr} : 0.04 rad

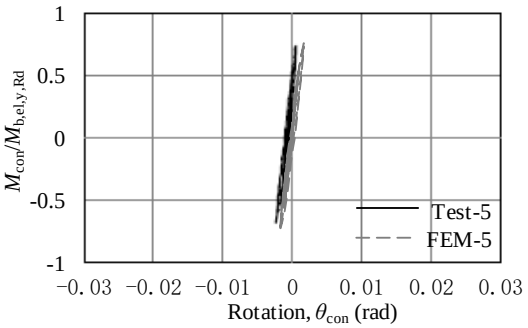

(e) Test-5 S355-OSH-WS-FP, θ_{dr} : 0.02 rad

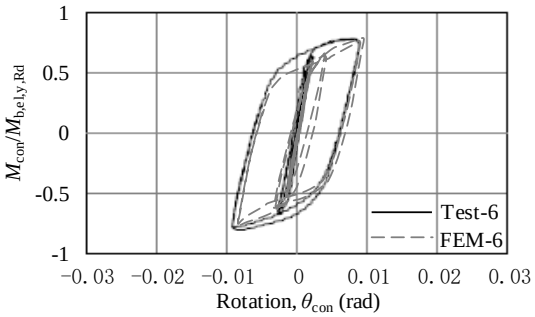

(f) Test-6 S235-NSH-NS-FP, θ_{dr} : 0.03 rad

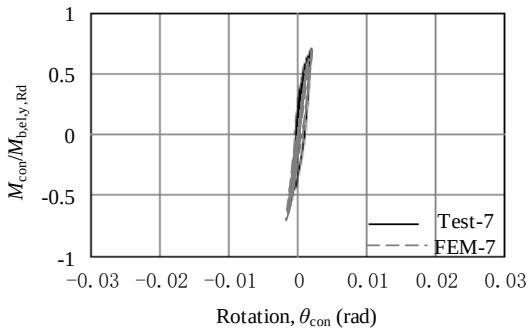

(g) Test-7 S355-NSH-NS-FP, θ_{dr} : 0.02 rad

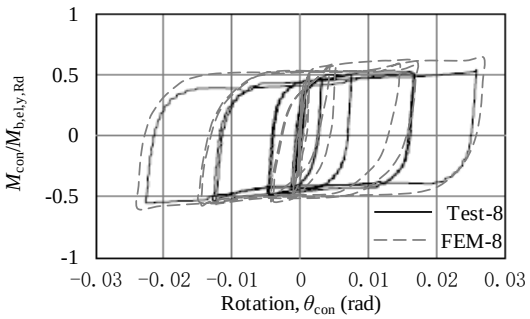

(h) Test-8 S235-OSH-NS-HP, θ_{dr} : 0.04 rad

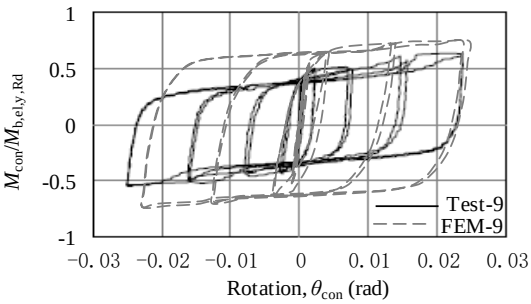

(i) Test-9 S355-OSH-WS-HP, θ_{dr} : 0.04 rad

Fig. 6 Normalised moment-rotation curves of nine tests

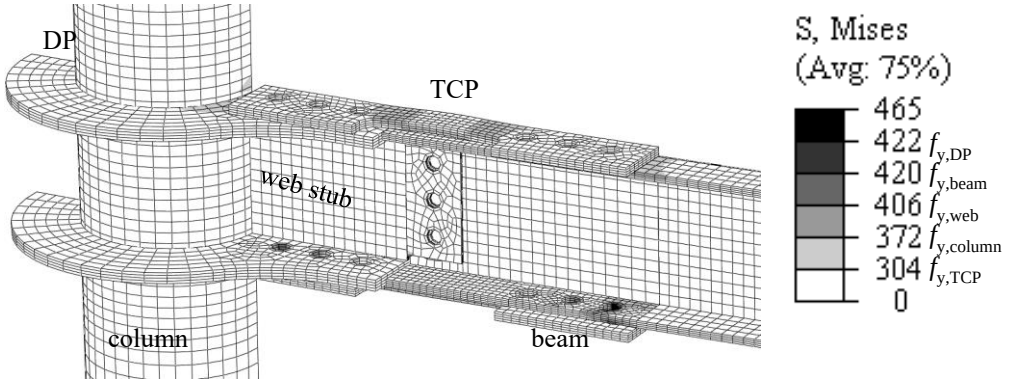

(a) FEM-6 S235-NSH-NS-FP (θ_{dr} : +0.03 rad)

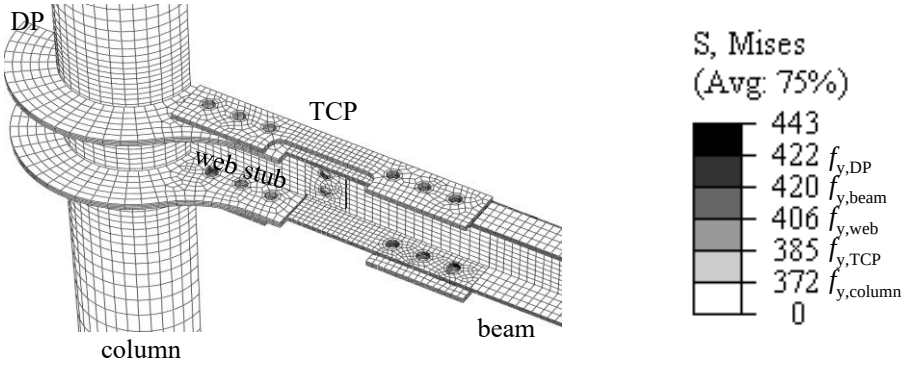

(b) FEM-7 S355-NSH-NS-FP (θ_{dr} : +0.02 rad)

Fig. 7 Mises stress contours of FEM-6 and FEM-7

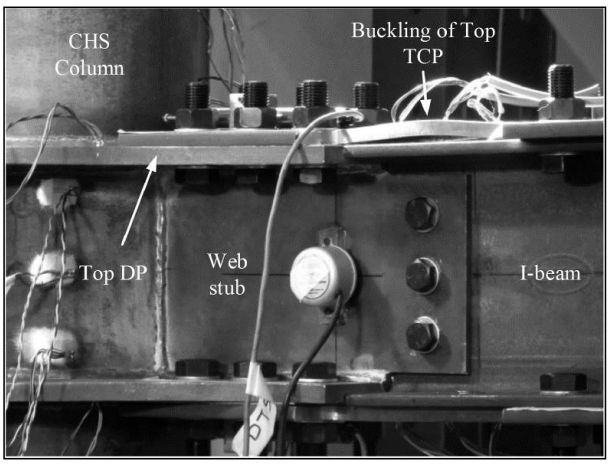

Fig. 8 Buckling of top TCP in Test-6 [20]

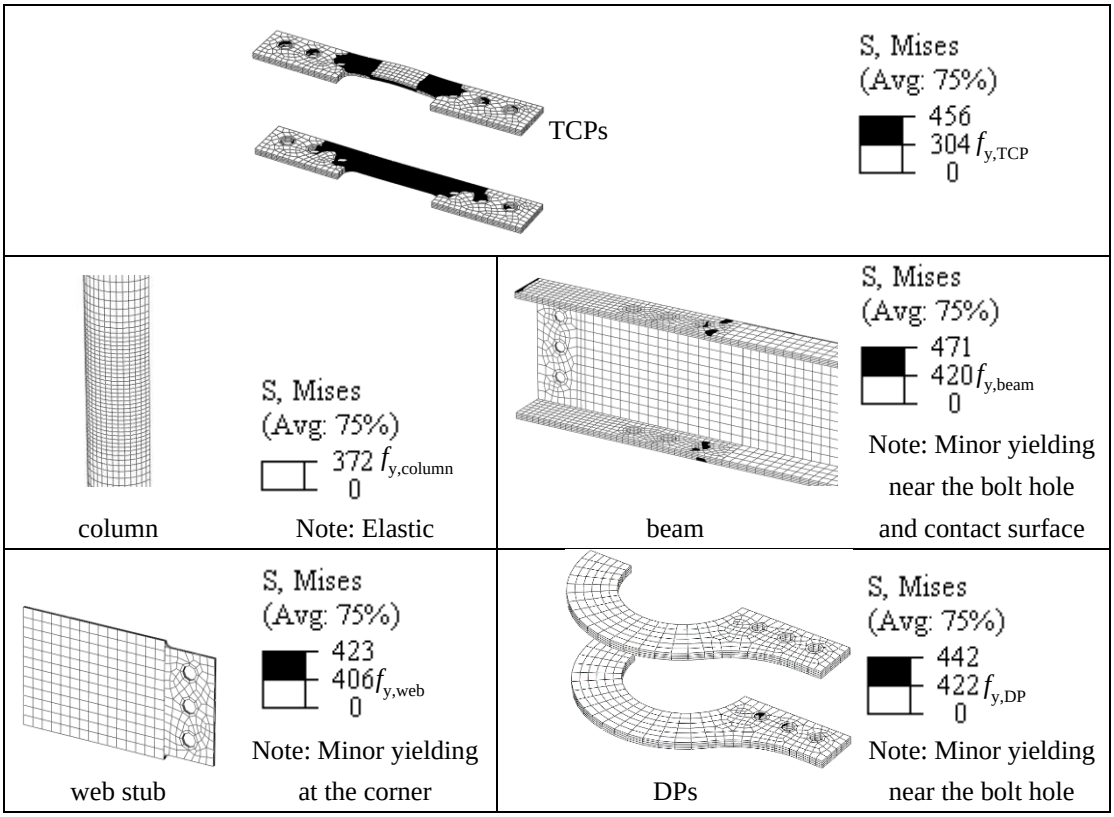

Fig. 9 Mises stress contours of main components in FEM-1 S235-OSH-NS-FP (θ_{dr} : +0.04 rad)

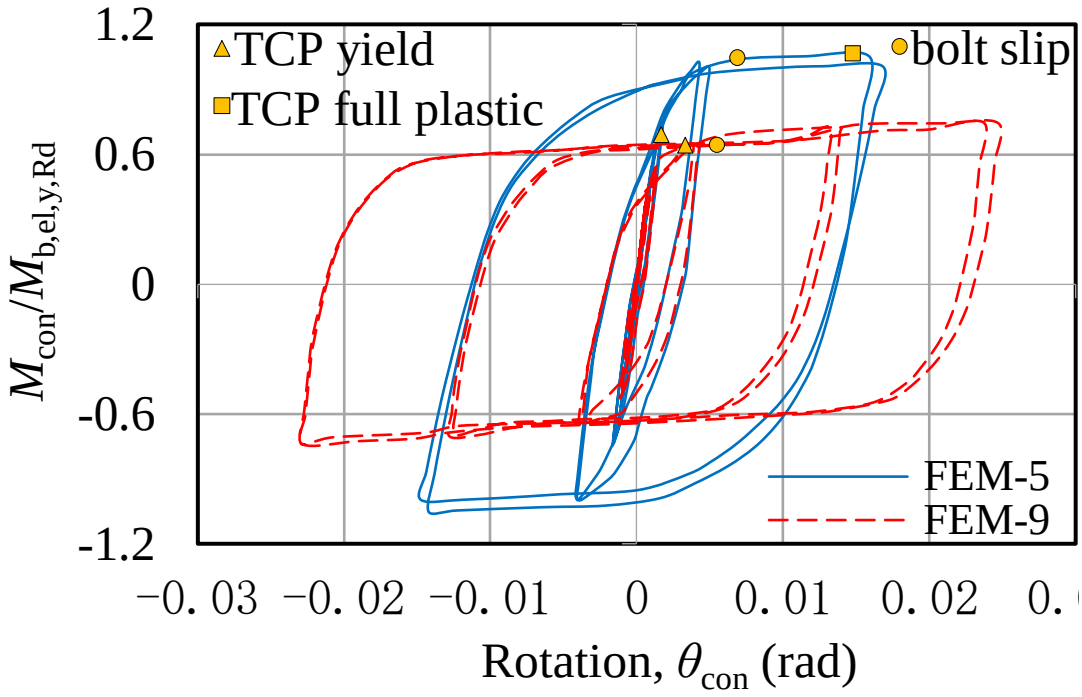

Fig. 10 Normalised moment-rotation curves of FEM-5 and FEM-9, θ_{dr} 0.04 rad

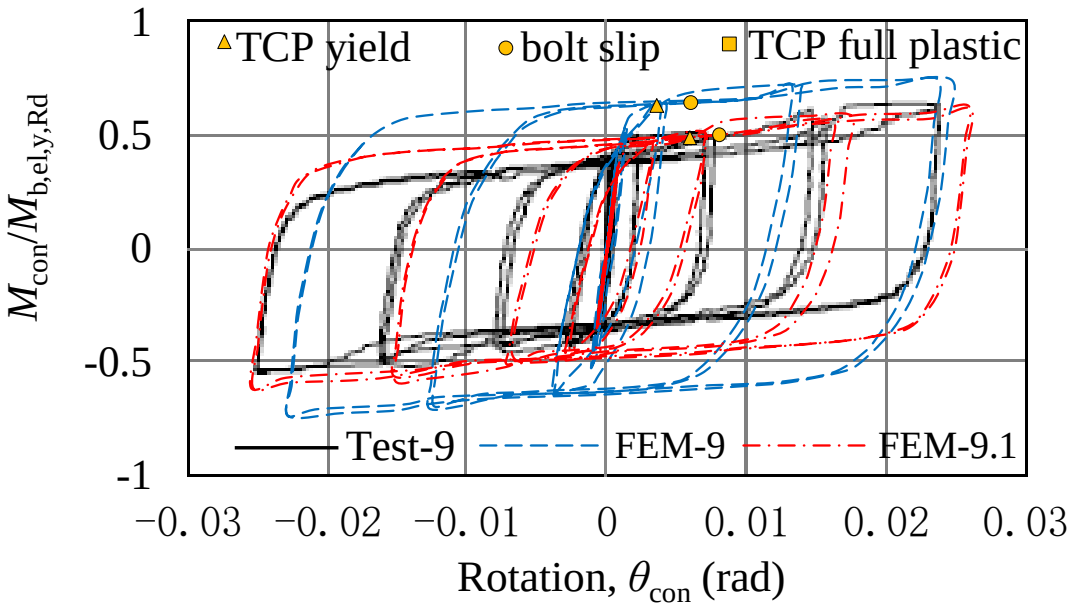

Fig. 11 Normalised moment-rotation curves of Test-9, FEM-9 and FEM-9.1, θ_{dr} 0.04 rad

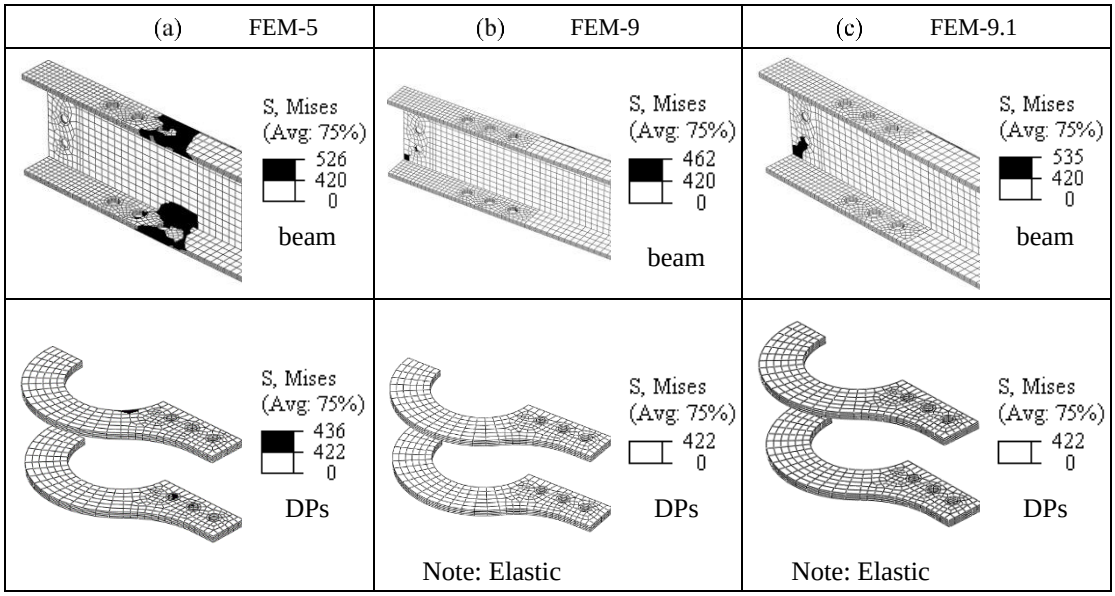

Fig. 12 Mises stress contours of beam and DPs in FEM-5, FEM-9, FEM-9.1 (θ_{dr} : +0.04 rad)

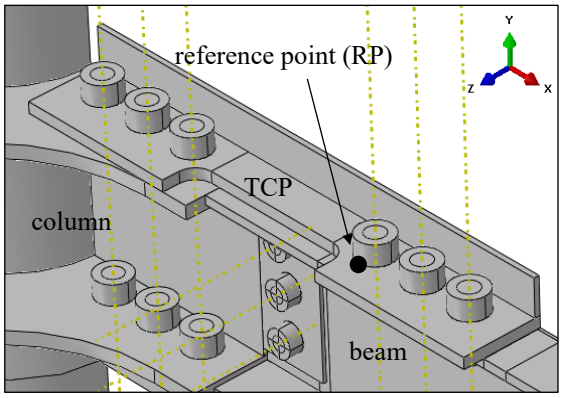

Fig. 13 RP was defined to describe relative displacement between bolt and TCP

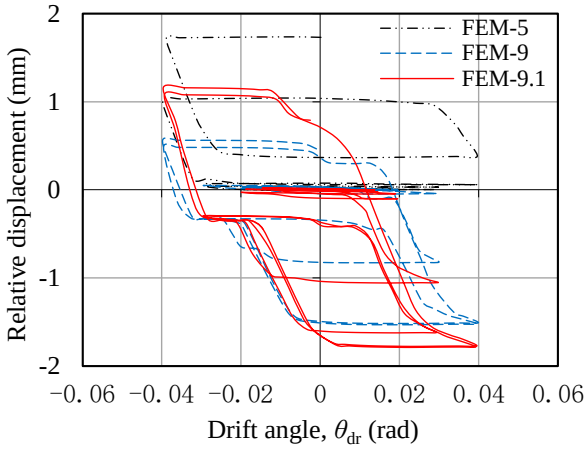

Fig. 14 Relative displacement between bolt and TCP in FEM-5, FEM-9, FEM-9.1

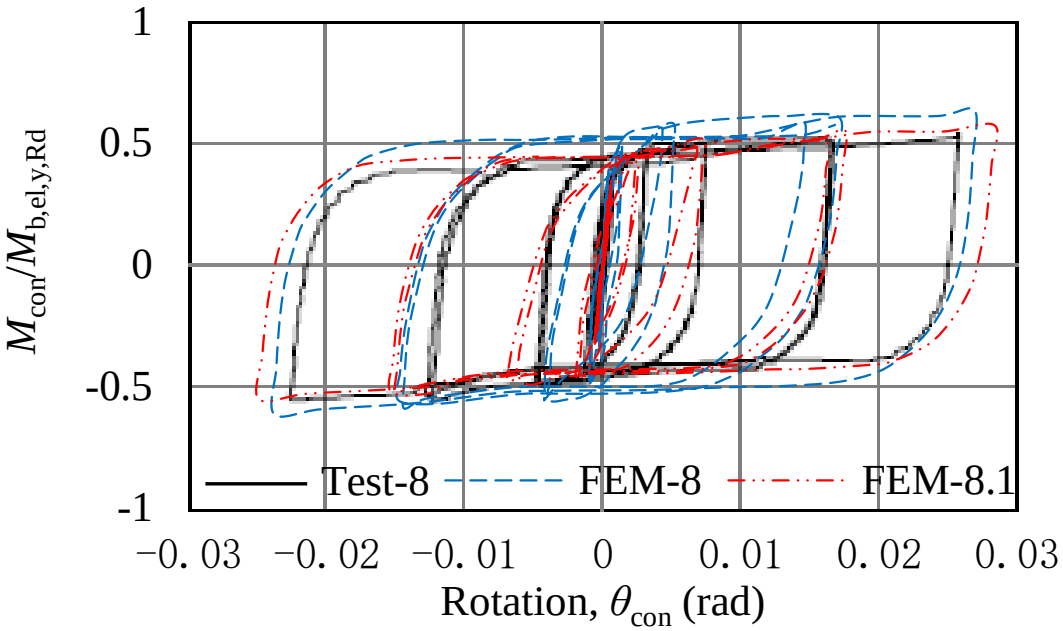

Fig. 15 Normalised moment-rotation curves of Test-8, FEM-8 and FEM-8.1, 29 cycles

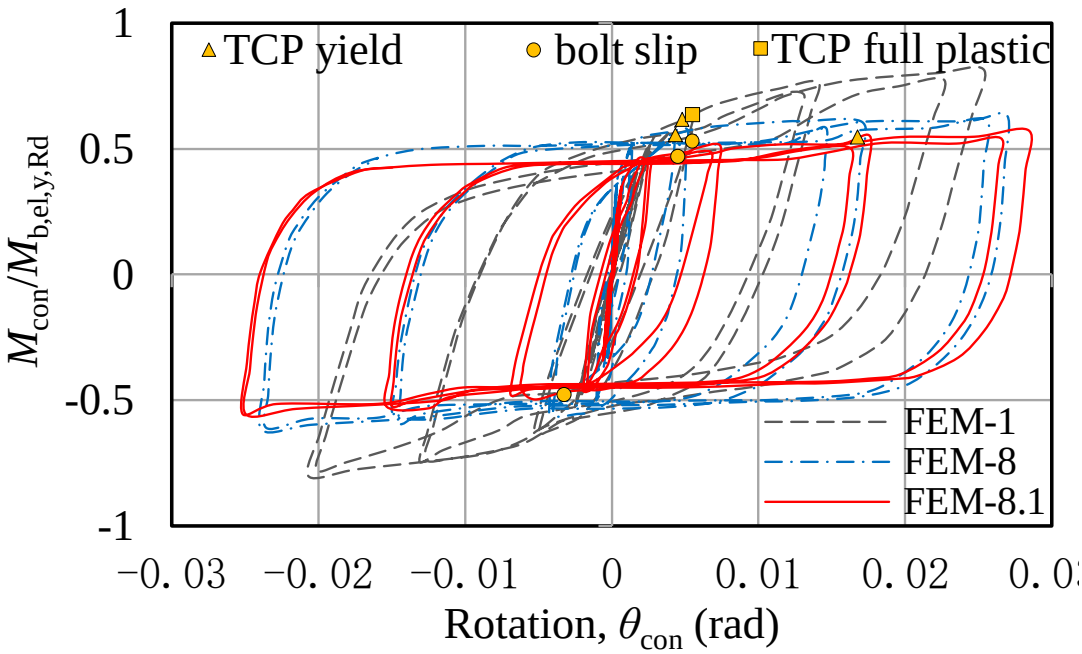

Fig. 16 Normalised moment-rotation curves of FEM-1, FEM-8, FEM-8.1, θ_{dr} 0.04 rad

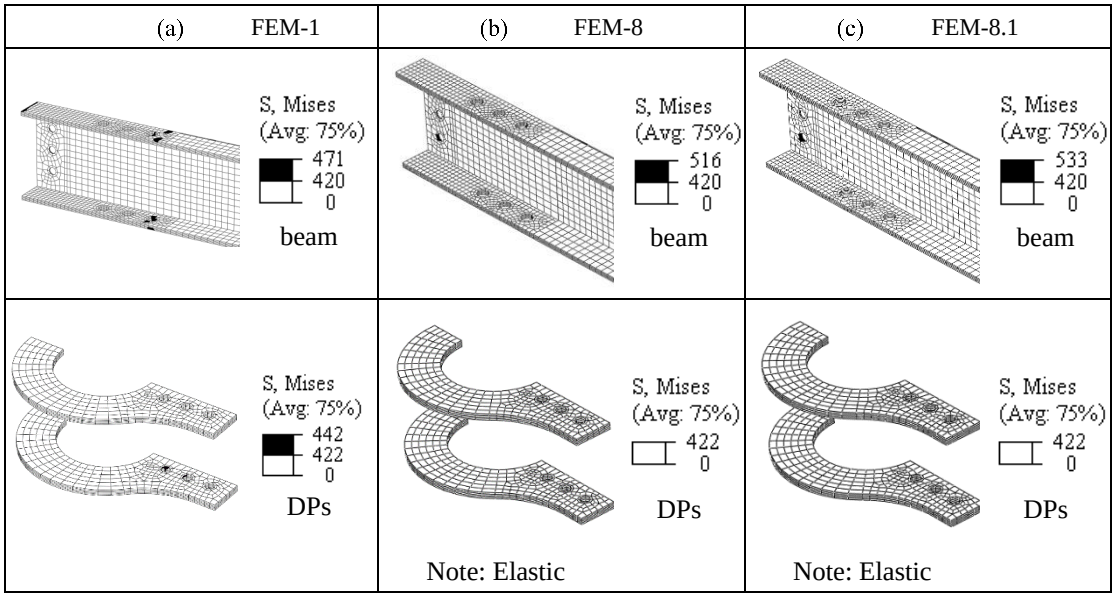

Fig. 17 Mises stress contours of beam and DPs in FEM-1, FEM-8, FEM-8.1 (θ_{dr} : +0.04 rad)

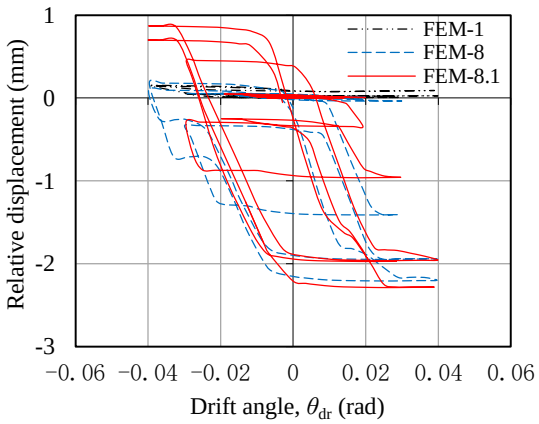

Fig. 18 Relative displacement between TCP's bolt and bolt hole in FEM-1, FEM-8, FEM-8.1

(a) Oversized holes in FEM-2 (b) Normal holes in FEM-3 (c) Slotted holes in FEM-3.1

Fig. 19 The sketches of TCP in FEM-2, FEM-3, FEM-3.1

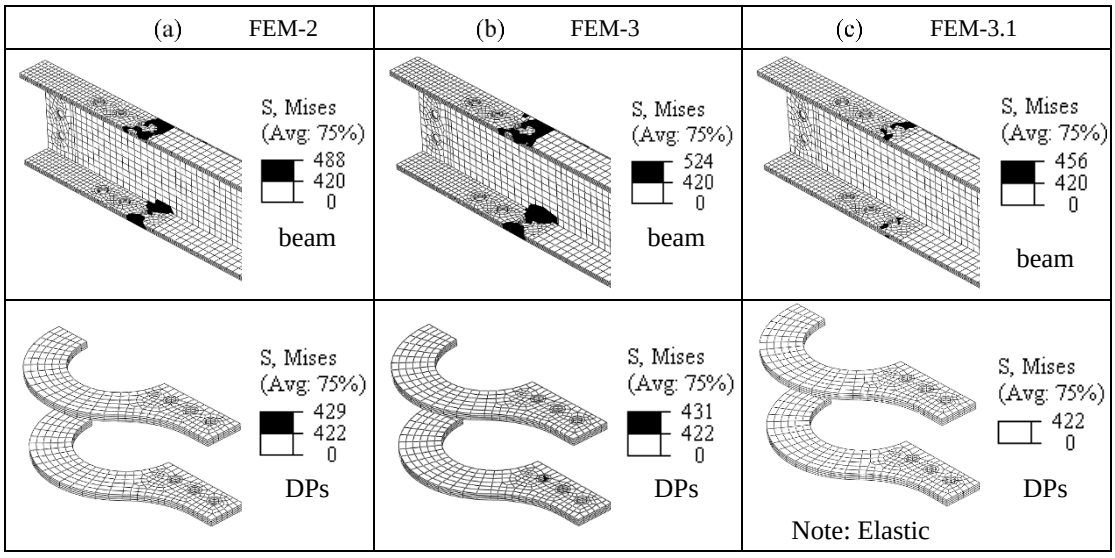

Fig. 20 Mises stress contours of beam and DPs in FEM-2, FEM-3, FEM-3.1 (θ_{dr} : +0.04 rad)

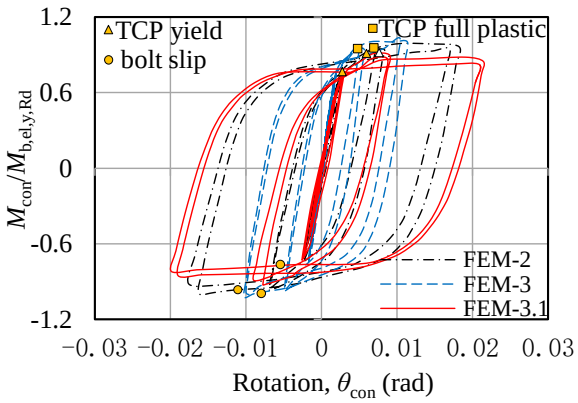

Fig. 21 Normalised moment-rotation curves of FEM-2, FEM-3, FEM-3.1, θ_{dr} 0.04 rad

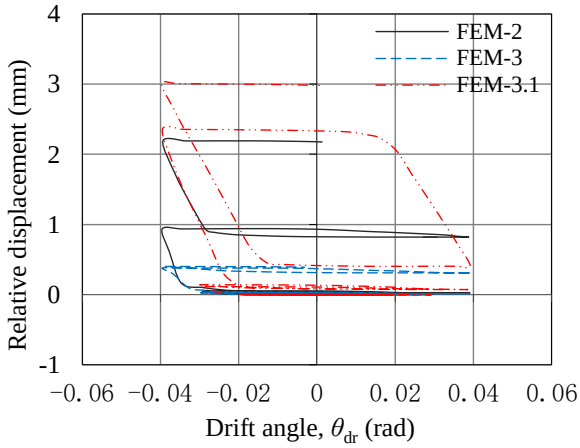

Fig. 22 Relative displacement between TCP's bolt and bolt hole in FEM-2, FEM-3, FEM-3.1

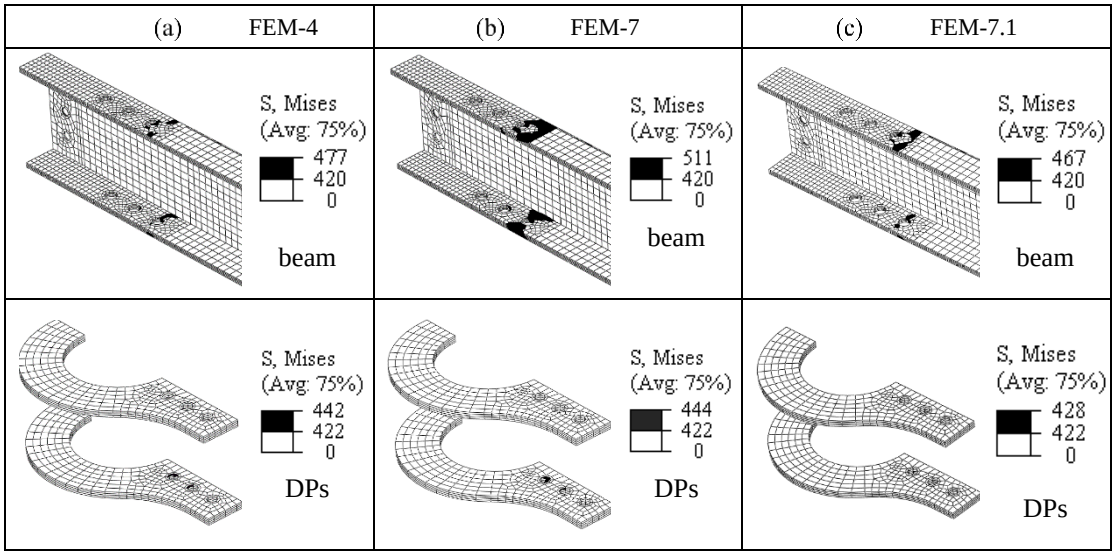

Fig. 23 Mises stress contours of beam and DPs in FEM-4, FEM-7, FEM-7.1 (θ_{dr} : +0.04 rad)

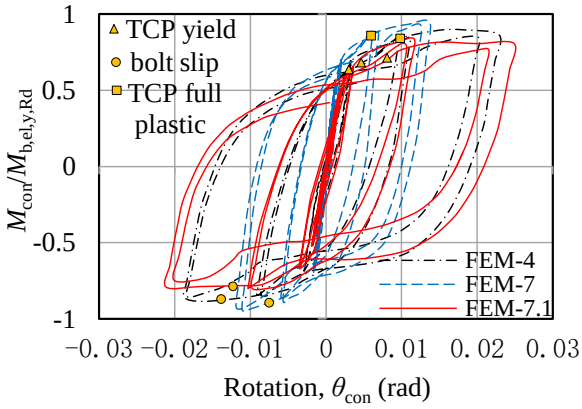

Fig. 24 Normalised moment-rotation curves of FEM-4, FEM-7, FEM-7.1, θ_{dr} 0.04 rad

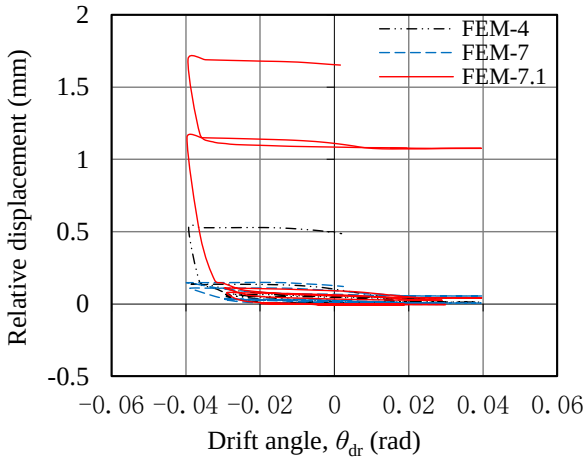

Fig. 25 Relative displacement between TCP's bolt and bolt hole in FEM-4, FEM-7, FEM-7.1

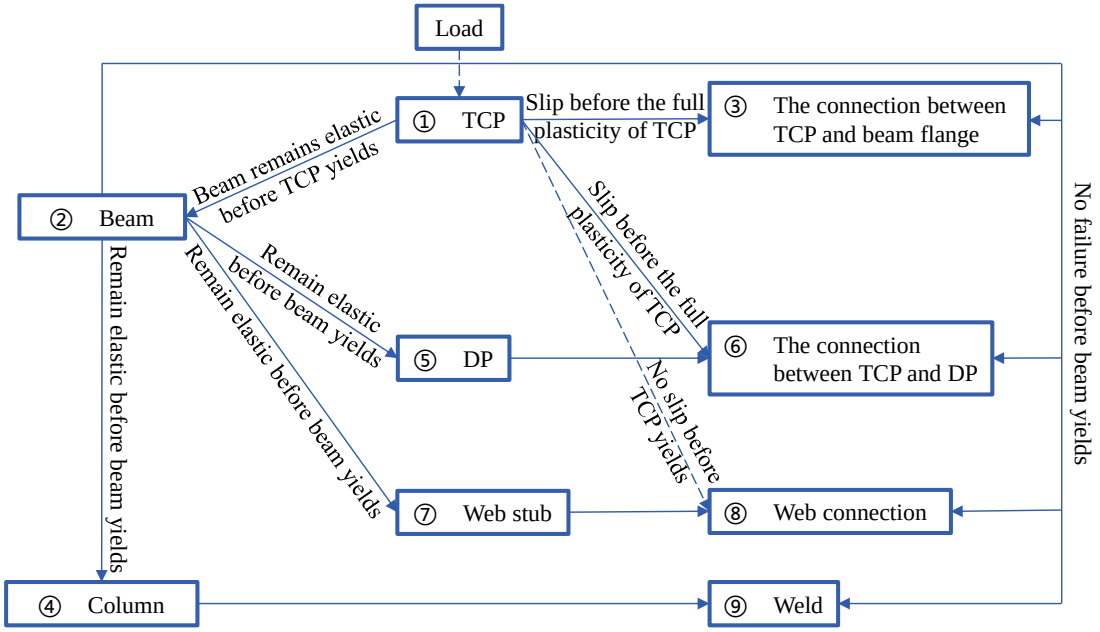

Fig. 26 Design flow

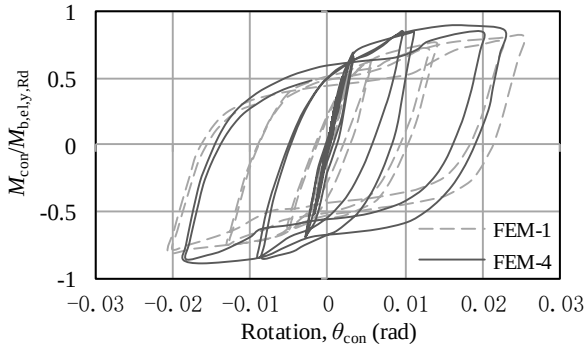

Fig. 27 Normalised moment-rotation curves of the connection in FEM-1, FEM-4, θ_{dr} 0.04 rad

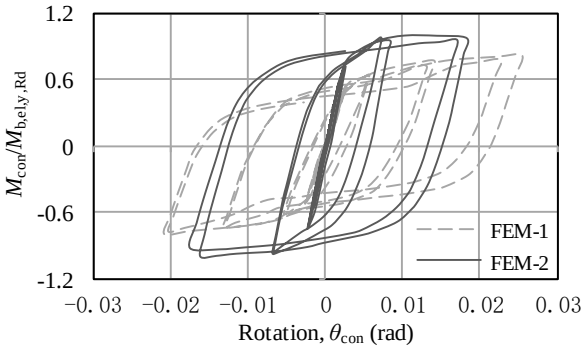

Fig. 28 Normalised moment-rotation curves of the connection in FEM-1, FEM-2, θ_{dr} 0.04 rad

Table 1 Tests titling according to the type of TCPs used in the test specimens [20]

	Test title	Type of Tapered Cover Plates (TCPs)			
		Steel grade	Size of bolt-holes	Use of stiffeners (Yes/No)	Bolts preload force
1	S235-OSH-NS-FP	S235	Oversized	No	Full
2	S235-OSH-WS-FP	S235	Oversized	Yes	Full
3	S235-NSH-WS-FP	S235	Normal	Yes	Full
4	S355-OSH-NS-FP	S355	Oversized	No	Full
5	S355-OSH-WS-FP	S355	Oversized	Yes	Full
6	S235-NSH-NS-FP	S235	Normal	No	Full
7	S355-NSH-NS-FP	S355	Normal	No	Full
8	S235-OSH-NS-HP	S235	Oversized	No	Half
9	S355-OSH-WS-HP	S355	Oversized	Yes	Half

Table 2 Key results from the tensile coupon tests [21]

Coupon	E (N/mm^2)	f_y (N/mm^2)	ε_y	f_u (N/mm^2)	ε_u
I-beam	203000	420	0.00207	560	0.13175
CHS Column	213000	372	0.00176	510	0.15549
Diaphragm Plate	215000	422	0.00196	557	0.16752
Web Stub	207000	406	0.00197	570	0.13795
S355 TCP	197000	385	0.00195	542	0.12842
S235 TCP	212000	304	0.00143	488	0.19559

Table 3 Loading protocol

Cycle number	Drift angle θ_{dr} (rad)	Vertical displacement d_a (mm)
1-6	±0.00375	±7.5
7-12	±0.005	±10
13-18	±0.0075	±15
19-22	±0.01	±20
23-24	±0.015	±30
25-26	±0.02	±40
27-28	±0.03	±60
29-30	±0.04	±80

Table 4 Initial rotational stiffness of the joints

Test number	Test title	Initial rotational stiffness of the joint $S_{j,ini}$ (kN·m/mrad)		Classification
		test	FEM	
1	S235-OSH-NS-FP	7.27	8.10	
2	S235-OSH-WS-FP	7.97	8.49	
3	S235-NSH-WS-FP	8.47	8.50	
4	S355-OSH-NS-FP	8.06	8.38	
5	S355-OSH-WS-FP	8.67	8.47	Semi-rigid
6	S235-NSH-NS-FP	7.96	8.46	
7	S355-NSH-NS-FP	7.78	8.43	
8	S235-OSH-NS-HP	7.56	8.30	
9	S355-OSH-WS-HP	8.38	8.37	

Table 5 Joint moment of nine tests

Test number	Test title	Maximum joint moment $M_{con,max}$ (kN·m)		Normalised maximum joint moment $M_{con,max}$ / $M_{b,pl,y,Rd}$	
		test	FEM	test	FEM
1	S235-OSH-NS-FP: 30 cycles	88.1	95.7	0.61	0.66
2	S235-OSH-WS-FP: 28 cycles	99.2	113.7	0.68	0.78
3	S235-NSH-WS-FP: 30 cycles	124.7	121.0	0.86	0.83
4	S355-OSH-NS-FP: 30 cycles	99.6	105.6	0.69	0.73
5	S355-OSH-WS-FP: 26 cycles	86.5	89.1	0.60	0.61
6	S235-NSH-NS-FP: 28 cycles	93.8	91.8	0.65	0.63
7	S355-NSH-NS-FP: 26 cycles	83.4	82.6	0.58	0.57
8	S235-OSH-NS-HP: 29 cycles	65.9	74.6	0.45	0.51
9	S355-OSH-WS-HP: 30 cycles	74.8	87.8	0.52	0.61

Table 6 Accumulated energy dissipation of joints

Test number	Test title	Cycle number	Accumulated energy dissipation (kN·m·rad)	
			test	FEM
1	S235-OSH-NS-FP	30	12.76	14.17
2	S235-OSH-WS-FP	28	3.23	2.91
3	S235-NSH-WS-FP	30	8.85	7.58
4	S355-OSH-NS-FP	30	11.41	12.86
5	S355-OSH-WS-FP	26	0.23	0.18
6	S235-NSH-NS-FP	28	3.65	3.70
7	S355-NSH-NS-FP	26	0.34	0.18
8	S235-OSH-NS-HP	29	12.76	13.56
9	S355-OSH-WS-HP	30	16.06	18.96